applied sciences

MDPI

Article

Structural Optimization and Thermal Performance Analysis of a Bio-Inspired Leaf-Vein Liquid Cooling System for Lithium-Ion Batteries: A Case Study of Agricultural Electric Forklifts

Zinan Ye [1,2], Dapeng Ye [1,2], Yuzheng Wu [1,2] and Bing Fang [1,2,*]

[1] College of Mechanical and Electrical Engineering, Fujian Agriculture and Forestry University, Fuzhou 350100, China; 52312040046@fafu.edu.cn (Z.Y.); ydp@fafu.edu.cn (D.Y.); yuzhengwu1214@gmail.com (Y.W.)
[2] Fujian Key Laboratory of Agricultural Information Sensing Technology, Fuzhou 350100, China
* Correspondence: fangbing@fafu.edu.cn

Abstract

To improve the thermal management performance of lithium-ion batteries under high discharge rates and complex operating conditions, a bidirectional parallel bionic flow-channel cooling plate is proposed, with agricultural electric forklifts taken as the representative application background. Numerical simulations were first carried out to compare the heat dissipation characteristics of a conventional leaf-vein flow channel, a unidirectional parallel bionic leaf-vein flow channel, and a bidirectional parallel bionic leaf-vein flow channel. On this basis, the effects of structural parameters on the thermal performance of the liquid cooling plate were systematically investigated using a single-factor analysis method. Furthermore, an orthogonal optimization experiment was performed for four major influencing factors. The results indicate that the unidirectional parallel bionic leaf-vein flow channel improved the coolant coverage relative to the conventional leaf-vein structure; however, owing to the one-sided coolant supply mode, a high-temperature retention zone tended to appear at the end of the channel. In contrast, the bidirectional parallel bionic design effectively alleviated this problem by supplying coolant synchronously from both sides. The main channel width, branch channel width, total channel height, and branch inclination angle were identified as the dominant factors affecting heat dissipation performance. Under the optimized structure and operating condition, the maximum temperature and temperature difference of the battery module were reduced to 29.85 °C and 4.48 °C, respectively.

Keywords: agricultural electric forklift; battery thermal management; bidirectional parallel bio-inspired leaf-vein flow channel; orthogonal design; parameter optimization

Check for updates

Academic Editor: Nikolaos Koukouzas

Received: 9 March 2026
Revised: 12 April 2026
Accepted: 23 April 2026
Published: 27 April 2026

Copyright: © 2026 by the authors. Licensee MDPI, Basel, Switzerland. This article is an open access article distributed under the terms and conditions of the Creative Commons Attribution (CC BY) license.

1. Introduction

With the increasing severity of global environmental problems, new energy technologies have gradually become a key driving force for industrial transformation across various sectors [1]. In the transportation and off-road machinery fields in particular, electrified vehicles and equipment are being widely developed because of their environmental benefits and high efficiency. Among them, electric forklifts are increasingly adopted in both agricultural and industrial applications [2]. As an important type of new energy vehicle, off-road electric forklifts have attracted growing attention owing to their high efficiency and environmental benefits [3]. However, under high-load and long-duration operating

conditions, battery thermal regulation remains one of the key factors restricting their performance and service life [4]. To ensure the safe and efficient operation of power battery packs, the overall battery temperature should generally be maintained within approximately 15–40 °C, while the maximum temperature difference inside the battery pack should be controlled within 5 °C [5,6]. Therefore, improving the heat dissipation efficiency of battery systems and maintaining battery packs within a stable temperature range have become important research topics.

As the core component of an electric forklift, the battery is highly sensitive to temperature, which directly affects its charge–discharge efficiency and service life. At present, battery thermal management systems (BTMSs) mainly include forced air cooling, heat pipe cooling, phase change material (PCM) cooling, liquid cooling, and hybrid cooling [7]. Considering the operating characteristics of agricultural off-road forklifts, such as high load, long working duration, irregular terrain, complex climatic environments, and frequent start-stop cycles, as well as the constraints of manufacturing and daily maintenance costs, selecting an appropriate BTMS is particularly important. Natural cooling and forced air cooling are simple and cost-effective, but their cooling capacity is limited and highly dependent on ambient temperature and air quality [8]. In high-power applications, they are often unable to meet the demand for efficient heat dissipation, resulting in non-uniform battery temperature distribution and accelerated battery degradation. PCM cooling, on the other hand, usually exhibits a delayed response to rapid changes in external thermal conditions. When the temperature rises sharply, PCM requires a certain amount of time to absorb heat and complete the phase transition, which makes it difficult to promptly dissipate the large amount of heat generated by the battery [9,10]. In addition, the high material cost and long-term stability issues of PCM also restrict its practical application. Over time, the phase transition characteristics of PCM may degrade, leading to a gradual decline in cooling performance, while system maintenance and material replacement remain relatively complex and costly [11]. By contrast, liquid cooling systems, benefiting from their closed-loop design, efficient heat transfer capability, and strong resistance to external environmental disturbances, can provide more stable and reliable thermal management under the harsh operating conditions of agricultural off-road forklifts. Even in hot, humid, or dusty environments, liquid cooling systems are capable of maintaining high heat dissipation efficiency, thereby ensuring the long-term stable operation of both the battery and the forklift system, reducing performance fluctuations and failures caused by environmental variations, and significantly lowering maintenance costs [11–13]. Therefore, liquid cooling is particularly suitable for battery thermal management under the demanding operating conditions represented by agricultural off-road electric forklifts.

To improve the thermal performance of liquid-cooled battery systems, a variety of cooling-plate channel structures have been proposed. Kong et al. [14] developed a novel divergent-channel liquid cooling plate different from the conventional straight-channel design and found that the divergent-channel structure exhibited superior heat transfer and hydraulic performance. They further reported that a dual-inlet single-outlet guiding channel could effectively reduce both the maximum temperature difference of the battery and the flow resistance of the cooling plate. Zhang et al. [15] designed an oblique-groove liquid cooling plate based on a straight-groove plate and compared their performances under different coolants, channel numbers, and mass flow rates, concluding that the oblique-groove design achieved better overall performance. Chen et al. [16] compared conventional I-type, Z-type, and U-type parallel-channel cooling plates, revealing that the I-type and Z-type plates showed similar performance and both outperformed the U-type design. Monika et al. [17] investigated six different channel configurations, including U-shaped, spiral, straight, pumpkin-shaped, serpentine, and hexagonal channels, and found that serpentine

and hexagonal channels could effectively improve battery temperature uniformity, whereas the pumpkin-shaped channel was beneficial for reducing flow resistance.

In recent years, bio-inspired channel structures have received increasing attention because of their potential to simultaneously improve cooling performance and flow distribution. Wang et al. [18] developed a liquid cooling plate with a bio-inspired spider-web channel structure for pouch batteries operating at an extreme discharge rate of 12C, and employed an orthogonal experimental design to investigate the effects of geometric parameters on both cooling and hydraulic performance. Their results showed that the enhancement in cooling performance was limited by channel width. Rong et al. [19] proposed a bio-inspired spider-web topology and found that the central included angle of the spider-web structure had little influence on battery temperature, whereas the channel width and channel spacing had more significant effects. Sheng et al. [20] designed a honeycomb liquid cooling plate and demonstrated that increasing the coolant flow rate and channel width could effectively improve heat transfer performance. Yang et al. [21] further proposed a novel honeycomb-channel liquid cooling plate combined with PCM and showed that the hybrid system outperformed a PCM-assisted straight-channel liquid cooling system. Deng et al. [22] designed a novel liquid cooling plate with leaf-shaped channels and investigated the influence of structural parameters on its performance, showing that the channel thickness had a relatively small effect on heat transfer but a significant effect on flow resistance. Tian et al. [23] designed a liquid cooling plate with a tree-branch channel structure and comparatively analyzed various geometric parameters. The optimal structural parameters were finally obtained using the NSGA-II genetic algorithm, thereby maximizing the overall performance of the cooling plate. Sheng et al. [24] also developed a liquid cooling plate with a novel serpentine channel structure and found that the dual-inlet dual-outlet configuration could effectively reduce the maximum battery temperature and improve temperature uniformity compared with the conventional single-inlet single-outlet design.

Despite these advances, the traditional single-inlet leaf-vein-inspired flow channel still suffers from pressure loss during coolant flow distribution, which makes it difficult to satisfy the demanding operating requirements encountered in applications such as agricultural electric forklifts under high load, frequent start-stop cycles, and complex environmental conditions [25,26]. In particular, during long-term high-power operation, a single-inlet structure may lead to uneven coolant distribution and an excessively long flow path, which weakens heat transfer performance and reduces cooling efficiency. In addition, insufficient cooling capacity near the end of the flow channel may cause local heat accumulation and the formation of a high-temperature retention zone [27,28]. To address this limitation, a bidirectional parallel bio-inspired leaf-vein flow channel was proposed in this study. By introducing two inlets and two outlets, the proposed structure increases the contact area between the battery and the flow channels, distributes the coolant into multiple parallel paths, reduces the flow resistance along a single path, and promotes a more uniform flow velocity in each branch channel.

In this work, numerical simulations were conducted to systematically compare the thermal performances of the conventional leaf-vein-inspired flow channel, the unidirectional parallel bio-inspired leaf-vein flow channel, and the bidirectional parallel bio-inspired leaf-vein flow channel. Special attention was paid to the effects of flow-channel configuration on the maximum battery temperature (Tmax), temperature uniformity (ΔT), and inlet–outlet pressure drop (ΔP). Furthermore, the influences of several structural parameters, including the main channel width (D), branch channel width (W), total channel height (H), number of branch channels (N), and branch angle (α), were investigated to reveal their coupled effects on heat dissipation performance. The optimal parameter combination was then determined, and the influence of inlet velocity (V) on thermal performance was further

examined under the optimized structure in order to identify the optimal operating condition. The main evaluation metrics considered in this study were the maximum temperature, maximum temperature difference, and channel pressure drop. Through these metrics, the thermal performances of different channel designs were comprehensively evaluated. The results of this study provide theoretical support for the design of bio-inspired liquid cooling channels and offer useful guidance for battery thermal management systems under complex operating conditions, such as those of agricultural electric forklifts.

2. Materials and Methods

2.1. Geometric Model of the BTMS

Inspired by the novel serpentine liquid cooling plate with dual inlets and dual outlets, as well as the bio-inspired leaf-vein flow channel, a bidirectional parallel bio-inspired leaf-vein flow channel was proposed to improve cooling efficiency, reduce battery heat accumulation, and enhance the temperature uniformity of the battery module. By increasing the contact area between the battery and the flow channels while simultaneously promoting a more uniform coolant distribution, the proposed structure aims to improve the heat transfer capability of the thermal management system.

The battery thermal management system (BTMS) model is shown in Figure 1. It consists of three prismatic lithium iron phosphate batteries (LFPBs) with identical specifications. Each LFPB has dimensions of 140 mm × 65 mm × 18 mm (length × height × thickness), a rated capacity of 15 Ah, and a nominal voltage of 3.2 V. The parameters of the single battery are listed in Table 1. The monomer lithium-ion battery parameters listed in this table are sourced from the battery specifications of the agricultural electric forklift used in this study. To maintain consistency with the simplification strategy adopted in this study, the positive and negative terminals of the batteries were neglected.

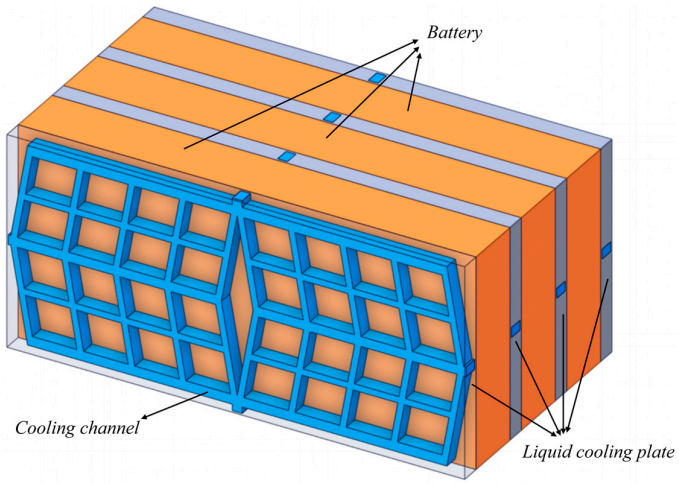

Figure 1. Battery thermal management model (BTMS).

A schematic diagram of the bidirectional parallel bio-inspired leaf-vein liquid cooling plate is shown in Figure 2. The cooling plate is made of aluminum, with dimensions of 140 mm × 65 mm × 6 mm, and is embedded on both sides of the LFPBs. The internal flow channels are arranged in a centrally symmetric manner along the upper, lower, left, and right directions. The thermophysical properties of the coolant and the liquid cooling plate are listed in Table 2 [29]. The internal cooling channel consists of a main channel and branch channels, and is formed by a parallel combination of outer large leaf veins and inner small leaf veins. The coolant enters the cooling plate from the left and right inlets and is then distributed through the branch channels into the inner and outer leaf-vein channels. After flowing through the cooling network and exchanging heat with the battery module,

the coolant gradually converges toward the upper and lower outlet channels and finally flows out of the plate. In this way, the bidirectional supply mode promotes a more uniform coolant distribution and helps reduce local heat accumulation in the downstream region. The extended axes of the inlet and outlet channels intersect at the center of the cooling plate. In the internal flow channel of the cooling plate, the main channel width is defined as D (mm), the branch channel width as W (mm), the total channel height as H (mm), the number of branch channels as N, and the angle between the branch channel and the main channel as α (°).

Table 1. Parameters of the single battery cell.

Parameter	Value
Battery type	15 Ah lithium iron phosphate battery
Capacity	15 Ah
Nominal voltage	3.2 V
Weight	0.35 kg
Dimensions	140 × 65 × 18 mm
Discharge cut-off voltage	2.25 V
Upper charging voltage	3.65 V
Continuous discharge current	3C

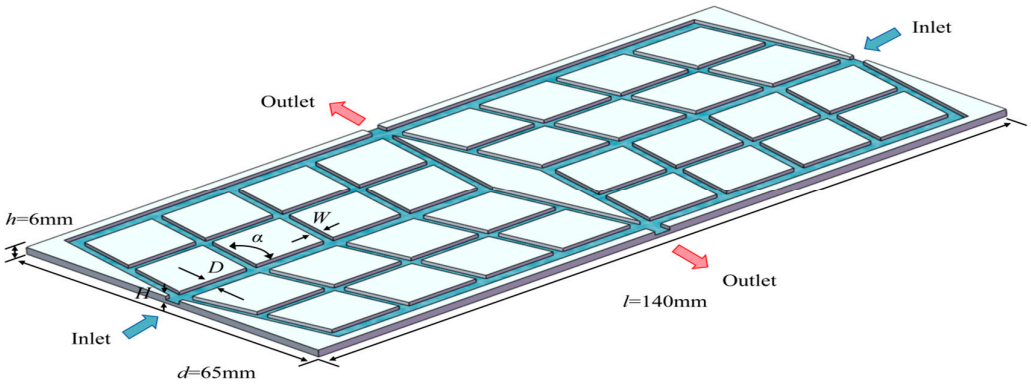

Figure 2. Bidirectional parallel bio-inspired leaf-vein liquid cooling plate.

Table 2. Thermal–physical properties of coolant and liquid cooling Plate [29].

Material	Density (kg/m^3)	Specific Heat Capacity (J/(kg·K))	Thermal Conductivity (W/(m·K))	Dynamic Viscosity (Pa·s)
Aluminum	2719	871	202.4	–
50% ethylene glycol/50% water	1071.11	3300	0.384	0.00339

2.2. Battery Heat Generation Model

During the charging and discharging processes, lithium-ion batteries generate heat due to ohmic resistance, polarization effects, and reversible entropy heat. To capture the temperature rise characteristics of the battery under different discharge rates with reasonable computational cost, the prismatic lithium iron phosphate battery is treated as a homogeneous continuous medium in this study. The internal microstructures, such as electrodes and separators, are neglected. An equivalent anisotropic thermal conductivity model is adopted, and the heat generation inside the battery is assumed to be uniformly distributed within the battery volume.

According to the energy conservation principle, the transient heat conduction governing equation in the battery domain can be written as [30]:

$$\rho_b C_{pb} \frac{\partial T_b}{\partial t} = \frac{\partial}{\partial x}\left(k_x \frac{\partial T_b}{\partial x}\right) + \frac{\partial}{\partial y}\left(k_y \frac{\partial T_b}{\partial y}\right) + \frac{\partial}{\partial z}\left(k_z \frac{\partial T_b}{\partial z}\right) + q_b \quad (1)$$

where ρ_b is the equivalent density of the battery (kg·m^{-3}); C_{pb} is the equivalent specific heat capacity (J·kg^{-1}·K^{-1}); k_x, k_y, and k_z represent the equivalent thermal conductivities along the three spatial directions (W·m^{-1}·K^{-1}); T_b denotes the battery temperature (K); and q_b is the volumetric heat generation rate (W·m^{-3}). This equivalent anisotropic conduction–volumetric heat generation model provides a good balance between computational efficiency and engineering accuracy and is widely used in battery thermal management simulations.

To characterize the heat generation term, the classical Bernardi heat generation model was adopted [31]. The total heat generation rate of the battery can be expressed as the sum of irreversible heat and reversible entropy heat

$$Q = I[(U - U_{ocv}) + T\left(\frac{dU_{ocv}}{dT}\right)] \quad (2)$$

where I is the battery current (A), U is the terminal voltage (V), U_{ocv} is the open-circuit voltage (V), T is the battery temperature (K), and $\frac{dU_{ocv}}{dT}$ is the entropy heat coefficient (V·K^{-1}).

If the ohmic resistance and polarization resistance are represented by an equivalent internal resistance R, the irreversible heat term can be approximated as I^2R. Thus, the total heat generation rate can be expressed as [32]:

$$Q \approx I(IR + T\frac{dU_{ocv}}{dT}) \quad (3)$$

To apply the heat generation in the CFD solver as a source term of the energy equation, the total heat generation rate is divided by the battery volume V_b, yielding the volumetric heat generation rate

$$q_V = \frac{Q}{V_b} \approx \frac{I^2R}{V_b} + \left(\frac{IT}{V_b}\right)\frac{dU_{(ocv)}}{dT} \quad (4)$$

where V_b is the battery volume (m^3). The volumetric heat source q_V is implemented directly as the source term in the energy equation of the battery domain to simulate the temperature distribution and temperature rise under different discharge rates. The volumetric heat generation rates listed in Table 3 were calculated based on the Bernardi heat generation model using Equations (2)–(4). These values were used as heat source inputs for the subsequent numerical simulations, and the reliability of the battery thermal model was further validated by comparing the simulated temperature evolution with the experimental results reported in Ref. [33].

Table 3. Heat generation per unit volume of battery at different discharge rates.

Discharge Rate (C)	Heat Generation Rate (W·m^{-3})
1	15,935
2	42,858
3	80,771

2.3. Validation of the Battery Model

To verify the feasibility of the battery heat generation model, a numerical simulation of a single battery cell was conducted under a 2C discharge rate at an ambient temperature

of 25 °C. The simulated temperature evolution was compared with the corresponding experimental results [33]. The comparison results are shown in Figure 3. The red line in the figure represents the experimental temperature results, while the black line represents the simulated temperature distribution results.

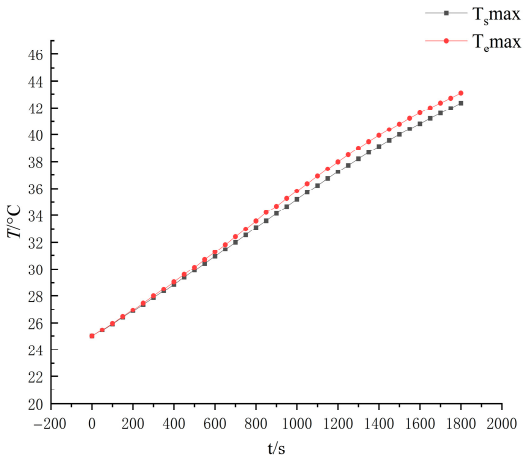

Figure 3. Temperature rise in a single battery: measured ($T_e$max) and calculated ($T_s$max).

Overall, the simulation results agree well with the experimental data throughout the discharge process. The maximum deviation occurs near the end of the discharge stage. The maximum deviation between the simulated and experimental results is within 0.28 °C. This discrepancy may mainly result from the simplifications introduced in the battery model and the fluctuation of the internal resistance during the discharge process.

The comparison indicates that the numerical model can accurately capture the thermal behavior of the battery under the considered operating condition. Therefore, the proposed battery heat generation model demonstrates good reliability and can be used for subsequent thermal simulations of the battery thermal management system.

2.4. Boundary Conditions

To evaluate the comprehensive performance of different flow-channel cooling plates in the battery thermal management system (BTMS), a solid–liquid conjugate heat transfer numerical model consisting of the battery, cooling plate, flow channel, and coolant was established. In all comparative simulations and parameter optimization cases, identical boundary conditions and heat generation loading methods were applied to ensure the comparability of different flow-channel configurations.

In practical applications, the operating ambient temperature of agricultural off-road telescopic forklifts generally ranges from −10 °C to 40 °C. In this study, an ambient temperature of 25 °C was adopted as the standard baseline condition to comparatively evaluate the heat dissipation performance of different flow-channel structures under a consistent environment. As listed in Table 4, at the initial simulation time, the temperatures of the battery, cooling plate, and coolant were set to the same value of T_0 = 25 °C. The coolant used in the simulation was a 50% ethylene glycol–water solution by mass fraction. The inlet of the flow channel was defined as a velocity inlet with an inlet velocity of V = 0.15 m·s^{-1}, while the outlet was specified as a pressure outlet with a pressure of P_{out} = 0 Pa.

Table 4. Boundary conditions used in the simulation.

Category	Parameter	Symbol (Unit)	Value
Fluid domain	Coolant type	-	50% ethylene glycol + 50% water (mass fraction)
	Inlet velocity	V ($m \cdot s^{-1}$)	0.15
	Inlet temperature	T_{in}(°C)	25
	Outlet pressure	P_{out} (pa)	0
Solid domain	Battery heat generation	q_v ($W \cdot m^{-3}$)	80,771
	Conjugate heat transfer	-	Enabled at fluid–solid interface
Ambient environment	Ambient temperature	T_∞(°C)	25
	Convective heat transfer coefficient	h ($W \cdot m^{-2} \cdot k^{-1}$)	5
Initial condition	Initial temperature	T_0(°C)	25

Conjugate heat transfer was applied between the battery, cooling plate, and channel walls. At the fluid–solid interface, the continuity of temperature and heat flux was enforced. For the external surfaces, a convective heat transfer boundary condition was imposed to represent the cooling effect of the surrounding air, with a heat transfer coefficient of $h = 5\,W \cdot m^{-2} \cdot K^{-1}$.

Under the cooling condition, the battery generated heat at a discharge rate of 3C, corresponding to a volumetric heat generation rate of $q_V = 80,771 W \cdot m^{-3}$. The maximum battery temperature T_{max} and temperature difference ΔT and ΔP at the 3C discharge condition were selected as the evaluation metrics for the subsequent grid independence verification.

2.5. Grid Independence Test

The three-dimensional BTMS model, including the battery module and liquid cooling plate with detailed geometry, was first established in SolidWorks 2024. The model was then imported into SpaceClaim for structure naming, interface handling, and necessary preprocessing operations. Finally, the model was meshed using Fluent Meshing, as shown in Figure 4. During meshing, the Poly-Hexcore method was employed, with the liquid cooling plate region discretized using a hybrid (Hexcore) mesh. For the fluid–solid coupling interface, a three-layer boundary layer mesh was applied to accurately capture the convective heat transfer between the coolant and the cooling plate walls.

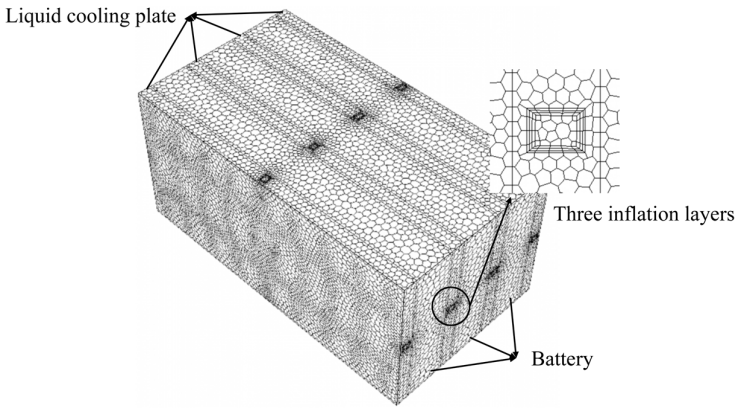

Figure 4. Mesh diagram.

To ensure the reliability of the numerical simulation results, a grid independence test was performed for the coupled liquid cooling plate–battery module model. The mesh configuration is shown in Figure 4. An excessively coarse mesh may lead to the loss of

flow details and inaccurate prediction of the temperature field, whereas an excessively fine mesh significantly increases computational cost.

In this study, five sets of computational meshes with different number of mesh cells were generated. The maximum battery temperature T_{max}, maximum temperature difference ΔT, and pressure drop of the flow channel ΔP were selected as evaluation metrics to examine the influence of mesh density on the simulation results.

As shown in Figure 5, with the increase in the number of mesh cells, the three evaluation metrics gradually converge. When the mesh number reaches 8.1×10^5 cells, the calculated values are T_{max} = 31.21 °C, ΔT = 5.12 °C, and ΔP = 74.12 Pa. Taking these values as reference, when the mesh number exceeds 8.1×10^5, the variation in T_{max} is less than 0.05 °C, the change in ΔT is smaller than 0.03 °C, and the difference in ΔP is less than 0.1 Pa.

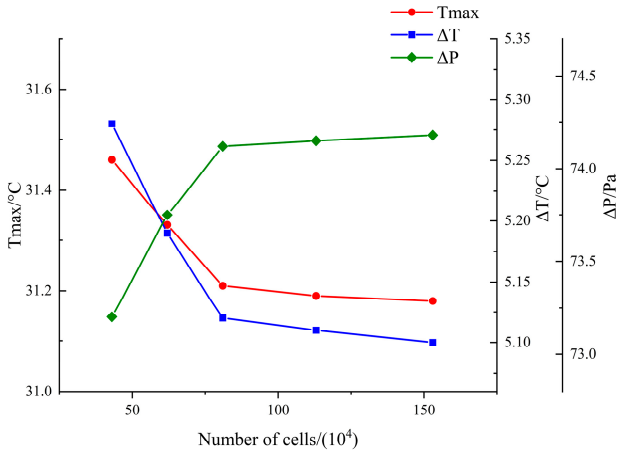

Figure 5. Grid independence verification.

These results indicate that further mesh refinement has a negligible influence on the simulation results. Considering both computational accuracy and efficiency, the mesh with approximately 8.1×10^5 cells was selected for all subsequent simulations.

3. Results and Discussion

3.1. Comparison of Heat Dissipation Performance for Different Bio-Inspired Leaf-Vein Flow Channel Cooling Plates

To further investigate the effect of bio-inspired flow channel structures on the thermal performance of the battery liquid cooling plate, a comparative analysis was conducted between the conventional leaf-vein flow channel, the unidirectional parallel bio-inspired leaf-vein flow channel, and the bidirectional parallel bio-inspired leaf-vein flow channel. Figure 6a,b show the structure of the conventional leaf-vein flow channel and the unidirectional parallel bio-inspired leaf-vein flow channel, respectively. Both flow channels feature a left-side single inlet and right-side dual outlets.

Numerical simulations were performed for all three flow channel structures under the same structural parameters and boundary conditions. The simulation results are shown in Figure 7. The conventional leaf-vein flow channel exhibited significantly higher values for both the maximum battery temperature T_{max} and the maximum temperature difference ΔT compared to the other two structures, with T_{max} reaching 32.28 °C and ΔT as high as 6.12 °C. These results indicate that the conventional structure has limited cooling coverage at the battery pack scale, and insufficient heat transfer in the downstream regions results in a significant temperature gradient.

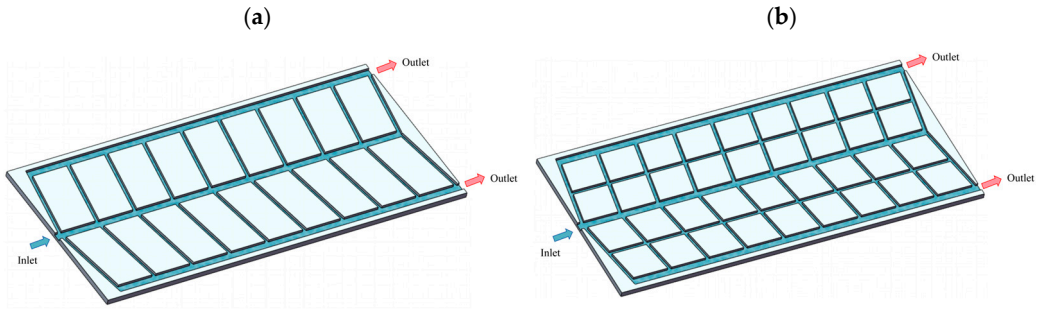

Figure 6. Schematic diagram of different bio-inspired structures, where (**a**) the structure of the conventional leaf-vein flow channel; (**b**) the unidirectional parallel bio-inspired leaf-vein flow channel.

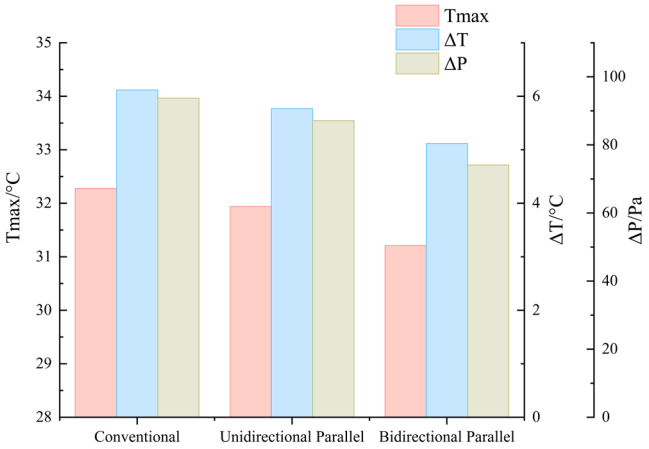

Figure 7. Comparison of heat dissipation performance for different structures.

The unidirectional parallel bio-inspired leaf-vein flow channel introduced a parallel structure based on the conventional leaf-vein flow channel, improving the flow distribution and cooling coverage in the central region of the battery. The simulation results show that T_{max} decreased to 31.94 °C and ΔT reduced to 5.77 °C, indicating a notable improvement in thermal management performance.

In comparison, the bidirectional parallel bio-inspired leaf-vein flow channel further optimized the distribution of fluid within the flow network by using a dual-inlet dual-outlet design, which significantly enhanced the overall heat transfer efficiency. The highest temperature for this structure was only 31.21 °C, with a maximum temperature difference of 5.12 °C, both representing the best performance among the three structures. In terms of pressure drop, the bidirectional parallel bio-inspired leaf-vein flow channel resulted in reductions of 19.65 Pa and 13.03 Pa compared to the other two flow channel structures.

3.2. Effect of Main Channel Width on Heat Dissipation Performance

After identifying the bidirectional parallel bio-inspired leaf-vein flow channel as the optimal design, a single-factor analysis was conducted to investigate the effect of each structural factor on heat dissipation performance. The analysis observed how different factor levels affected the thermal distribution and internal channel pressure of the BTMS. The parameter ranges for each factor were determined based on the findings of Albana et al. [34] and Niu et al. [35], which suggest that increasing geometric parameters within a certain range can improve coolant distribution and reduce flow resistance, thereby enhancing heat transfer performance. However, excessive enlargement of these parameters may lead to a decrease in flow velocity and a deterioration of heat transfer efficiency, while also taking into account the geometric proportion between the cooling plate and the flow channels, as well as manufacturing feasibility. Initially, a single-factor analysis

was conducted for the main channel width (D). The analysis was conducted under the conditions of W = 1.5 mm, H = 4 mm, N = 10, $\alpha = 80°$, and an inlet velocity of V = 0.15 m·s^{-1}, with D values of 1.5, 2, 2.5, and 3 mm selected for comparison.

As shown in Figure 8, with the increase in D, T_{max} decreased from 33.27 °C to 31.21 °C, ΔT decreased from 6.31 °C to 5.12 °C, and ΔP decreased from 102.35 Pa to 74.12 Pa. This indicates that increasing the main channel width improves both heat dissipation performance and reduces flow resistance.

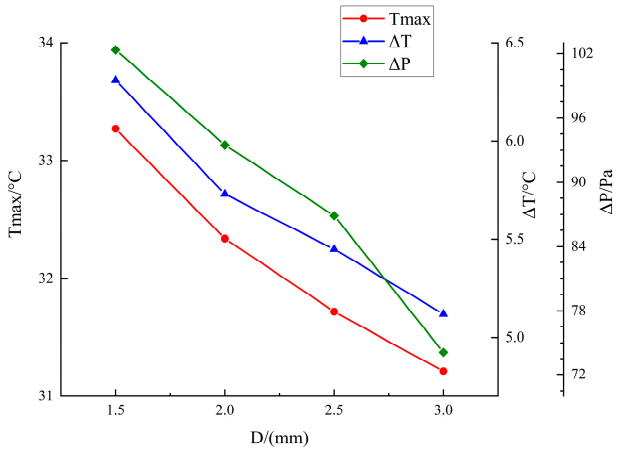

Figure 8. Variation in T_{max}, ΔT, and ΔP with main channel width D.

As shown in Figure 9, when the main channel width D is small (1.5 mm), high-temperature regions are more pronounced in the central and outlet areas of the battery pack, resulting in larger hotspot areas. As D increases, the high-temperature regions gradually shrink, and the temperature distribution becomes more uniform. This effect arises because the hydraulic diameter of the main channel increases, reducing frictional losses and pressure drop along the channel, which improves coolant distribution and flow uniformity. In addition, a larger main channel width decreases local velocity-induced shear losses, enhancing heat transfer efficiency at the battery surface. These findings indicate that selecting an appropriate main channel width can mitigate local hotspots and improve the overall thermal management performance of the battery pack, providing clear guidance for flow channel optimization.

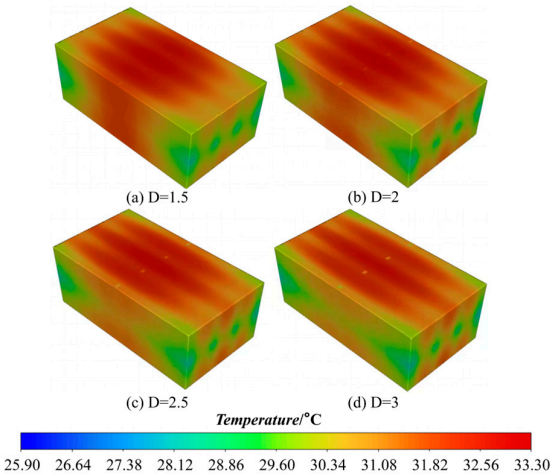

Figure 9. Temperature variation in battery for different main channel widths (mm).

Figure 10 further shows that, when D is small (1.5 mm), there are more significant pressure gradients and local pressure drops in the branch region and near the outlet.

However, when D increases to 3 mm, the local losses in the branch regions and the pressure gradients near the outlet are alleviated, resulting in a reduced overall pressure difference and improved cooling performance at the outlet. Therefore, within the scope of this study, D = 3 mm corresponds to the optimal overall performance, and selecting D = 3.0 mm is most suitable for subsequent studies.

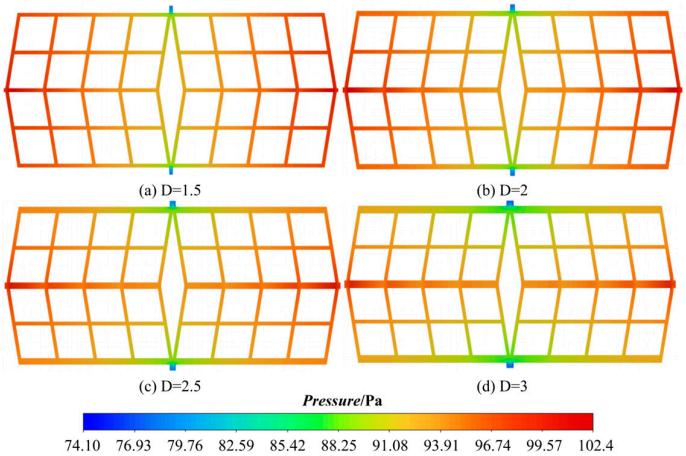

Figure 10. Variation in inlet and outlet pressure drop for different main channel widths (mm).

3.3. Effect of Branch Channel Width on Heat Dissipation Performance

After determining D = 3 mm as the optimal parameter for the main channel width, a further analysis was conducted to investigate the effect of the branch channel width (W) on the heat management performance of the liquid cooling plate. To ensure the accuracy of the single-factor analysis, the other structural parameters were kept constant: D = 3 mm, H = 4 mm, N = 10, $\alpha = 80°$, and an inlet velocity of V = 0.15 m·s^{-1}. Branch channel widths of W = 1, 1.5, 2, and 2.5 mm were selected for comparison.

As shown in Figure 11, with the increase in branch width W, both the maximum temperature Tmax and the temperature difference ΔT initially decrease but later show a slight rebound, while the pressure drop ΔP continuously decreases. This variation reflects the competition between enhanced heat transfer and reduced flow velocity. Wider branch channels improve coolant distribution, allowing heat to be more uniformly removed from the battery surface and reducing Tmax and ΔT; however, when W exceeds a certain range, local flow velocities decrease further, lowering convective heat transfer capacity and slightly increasing the temperature difference. Meanwhile, the wider branch channels reduce overall flow resistance, resulting in a continuous decrease in ΔP. Optimizing branch width thus requires balancing thermal management effectiveness and flow resistance to achieve uniform temperature distribution and efficient system operation.

Figure 12 shows a consistent phenomenon with this trend: When W = 1 mm, some branches experience weaker coolant distribution, and localized hotspots are more likely to form at the outlet side and the middle section. However, when W increases to 2 mm, the distribution of coolant in the branches improves, and the high-temperature zones are effectively suppressed.

Meanwhile, Figure 13 shows that increasing W significantly reduces the resistance at the branch points, leading to a decrease in the overall pressure drop. It is important to note that, when W becomes too large, the increased branch cross-section causes a decrease in the local average flow velocity. Although the resistance is lower, the convective heat transfer strength may not continue to improve, and the temperature control benefits start to exhibit diminishing returns, or even a slight rebound.

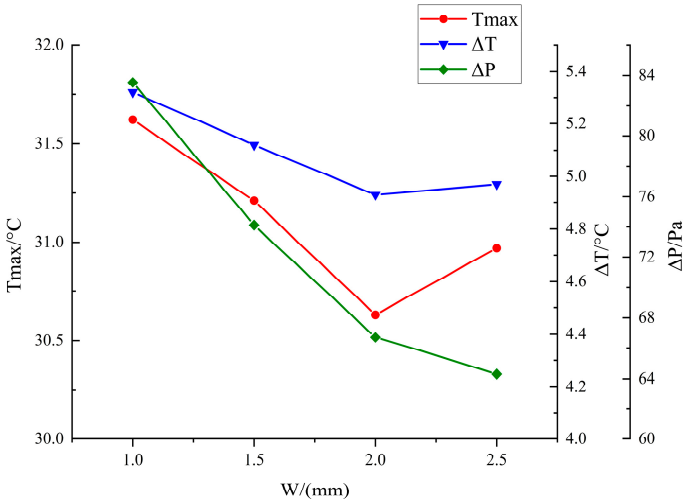

Figure 11. Variation in T_{max}, ΔT, and ΔP with branch channel width W.

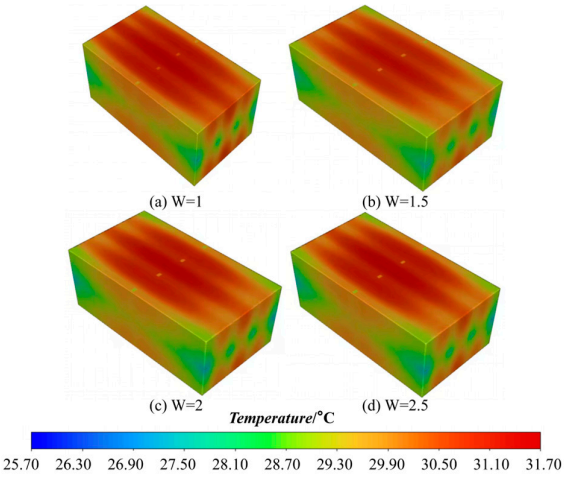

Figure 12. Temperature variation in battery for different branch channel widths (mm).

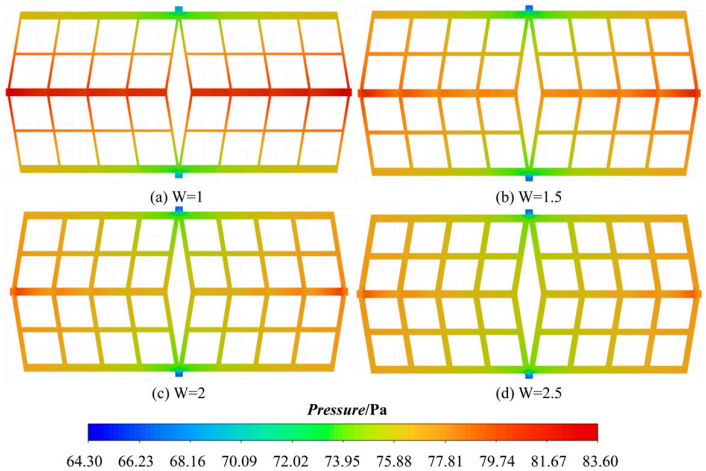

Figure 13. Variation in inlet and outlet pressure drop for different branch channel widths (mm).

3.4. Effect of Total Channel Height on Heat Dissipation Performance

Further investigation was conducted on the effect of the channel height (H) on the heat dissipation performance of the liquid cooling plate. The main channel width was set to D = 3 mm, the branch channel width to W = 2 mm, the number of branch channels to N = 10 N, and the angle between the branch and main channels to $\alpha = 80°$. The inlet velocity

was V = 0.15 m·s^{-1}. Under these conditions, numerical simulations were performed with different channel heights (H = 3 mm, 3.5 mm, 4 mm, 4.5 mm).

As shown in Figure 14, the effect of channel height on heat dissipation performance showed a consistent positive trend, unlike the effect of branch channel width. As H increased from 3 mm to 4.5 mm, T_{max} continuously decreased from 32.17 °C to 30.24 °C, a reduction of 1.93 °C (approximately 6.0%), while ΔT decreased from 5.91 °C to 4.68 °C, a reduction of 1.23 °C (approximately 20.8%). The pressure drop (ΔP) also gradually decreased to 63.45 Pa.

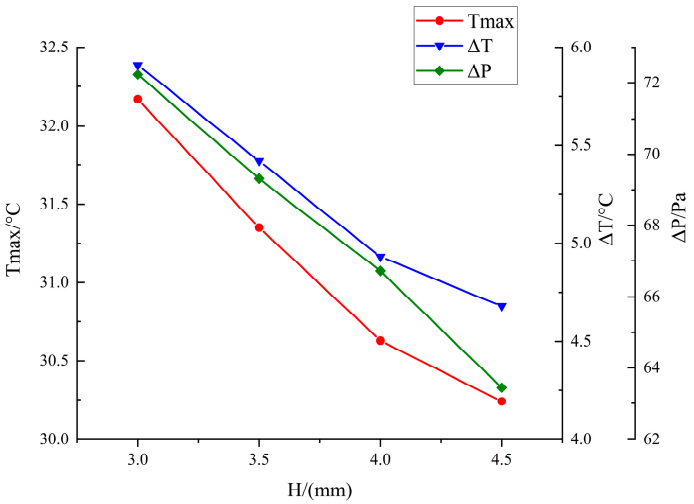

Figure 14. Variation in T_{max}, ΔT, and ΔP with total channel height H.

As shown in Figure 15, increasing the total channel height H causes high-temperature regions in the temperature contour to gradually shrink, and the color gradient becomes smoother, indicating more uniform heat removal. This effect is mainly due to the increased cross-sectional area of the channels, which allows a greater coolant flow, reduces local flow resistance, and improves the overall flow distribution in the channel network. A higher channel height also reduces the probability of local hotspots and improves heat transfer efficiency at the battery surface, providing concrete guidance for cooling plate design.

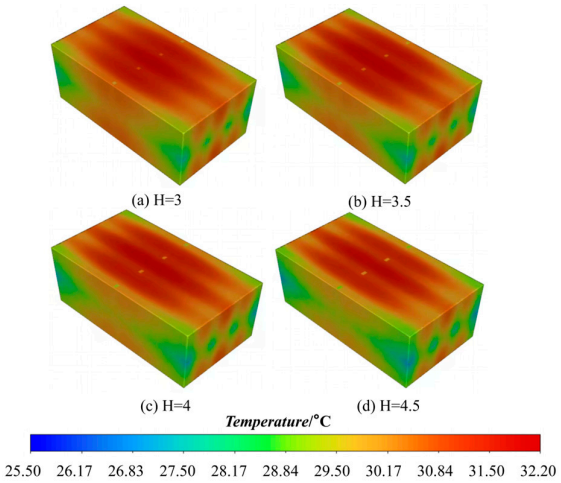

Figure 15. Temperature variation in battery for different total channel heights (mm).

Figure 16 further explains this dual improvement. Increasing H effectively increases the cross-sectional area of the channel and enhances the hydraulic diameter, which reduces frictional losses along the channel and weakens the pressure gradient, leading to a reduction in pressure drop. Under the same inlet velocity boundary condition, the flow network can

maintain a smoother flow state, reducing local energy dissipation and improving coolant distribution, which is consistent with the observed "shrinking of the high-temperature regions and smoother temperature fields."

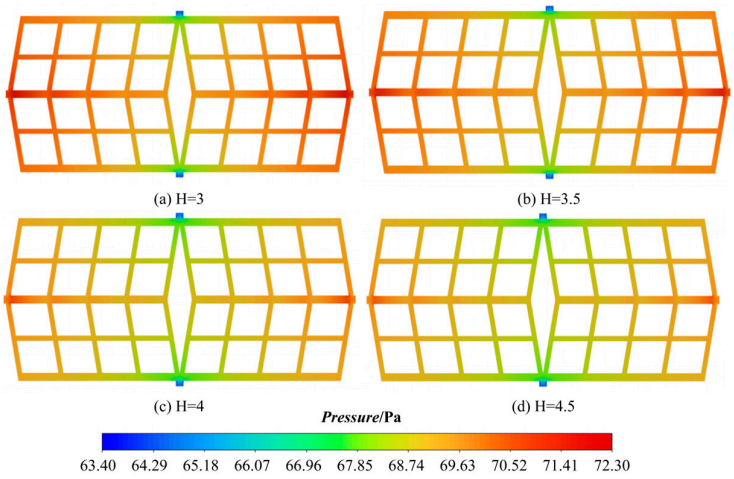

Figure 16. Variation in inlet and outlet pressure drop for different total channel heights (mm).

Both the line graph and contour analysis clearly indicate that H is beneficial for both temperature control and pressure drop. Therefore, H = 4.5 mm was selected as the optimal value, with a clear physical rationale.

3.5. Effect of Branch Channel Number on Heat Dissipation Performance

The number of branch channels (N) affects the coolant distribution within the flow channels and the heat transfer area between the coolant and the liquid cooling plate. Therefore, a further study was conducted to investigate the effect of branch channel number on the heat dissipation performance of the liquid cooling plate. The main channel width was set to D = 3 mm, the branch channel width to W = 2 mm, the channel height to H = 4.5 mm, the angle between the branch and main channels to $\alpha = 80°$, and the inlet velocity to $V = 0.15\ m{\cdot}s^{-1}$. The study analyzed the changes in maximum battery temperature (T_{max}), maximum temperature difference (ΔT), and pressure drop (ΔP) as N increased from 6 to 12.

As shown in Figure 17, with the increase in branch channel number N, the maximum temperature of the battery system first decreased and then increased. When N increased from 6 to 10, T_{max} decreased from 30.37 °C to 30.24 °C, and ΔT decreased from 4.78 °C to 4.68 °C. However, when N increased further to 12, Tmax increased to 30.32 °C, but due to the increase in the number of branches, ΔT continued to decrease slightly to 4.64 °C.

As shown in Figure 18, when the branch number N was small, the heat field exhibited a noticeable peak in areas with weak coverage. When N increased to 10, the cooling network's coverage density improved, effectively dispersing and reducing the hotspots. When N increased further to 12, the temperature distribution became more uniform (with a smaller temperature difference), but due to the further division of flow in each branch, the local flow velocity decreased, causing a slight increase in the peak temperature.

Figure 19 further illustrates that, as the number of branches increased, the accumulation of local losses at the bifurcation and confluence nodes became more apparent, resulting in a slight increase in pressure drop (ΔP), from 62.41 Pa to 63.92 Pa. The results of this study indicate that the change in the number of branch channels has a relatively small impact on the overall performance of the battery pack. Therefore, N = 10 N was selected as the optimized parameter for subsequent studies.

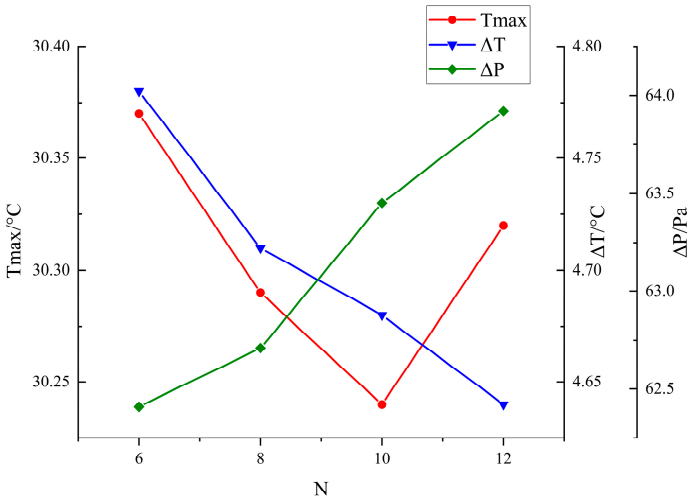

Figure 17. Variation in T_{max}, ΔT, and ΔP with branch channel number N.

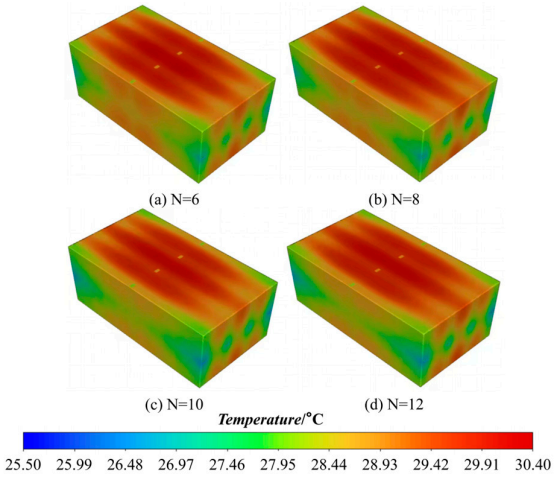

Figure 18. Temperature variation in battery for different branch channel numbers.

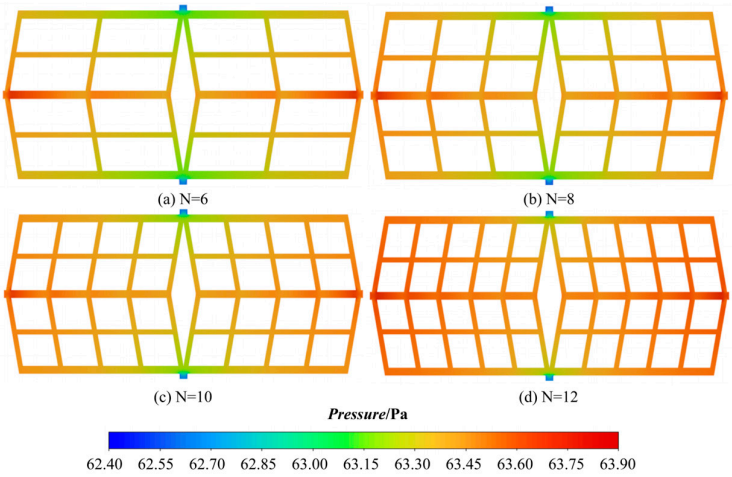

Figure 19. Variation in inlet and outlet pressure drop for different branch channel numbers.

3.6. Effect of Branch Channel Angle on Heat Dissipation Performance

The angle between the branch and main channels (α) has a certain impact on the heat dissipation performance of the flow channel plate. Therefore, with D = 3 mm, W = 2 mm, H = 4.5 mm, N = 10, and an inlet velocity of V = 0.15 m·s^{-1}, the effect of the branch channel angle (α) on heat dissipation performance was investigated as α increased from 65° to 80°.

As shown in Figure 20, with the increase in the branch angle α, the maximum battery temperature and temperature uniformity improved significantly. When α increased from 65° to 80°, Tmax decreased from 30.91 °C to 30.24 °C, a reduction of 0.67 °C (approximately 2.2%), while the maximum temperature difference (ΔT) decreased from 5.08 °C to 4.68 °C, a reduction of approximately 7.9%.

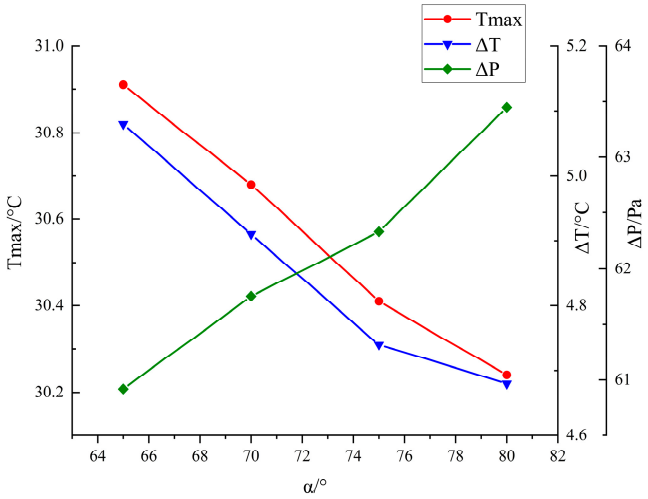

Figure 20. Variation in T_{max}, ΔT, and ΔP with branch channel angle α.

As shown in Figure 21, larger branch angles α facilitate the entry of coolant into the branches, enhancing network coverage and effectively mitigating thermal accumulation in the central region of the battery. As α increases, the intensity of hotspots in the middle and outlet regions gradually decreases. This effect occurs because a larger branch angle improves coolant distribution across the branches, increasing local heat transfer efficiency and reducing peak temperatures in the central region. Proper selection of the branch angle can optimize coolant flow paths, enhance temperature uniformity, and improve overall cooling system performance, providing practical guidance for bio-inspired flow channel design.

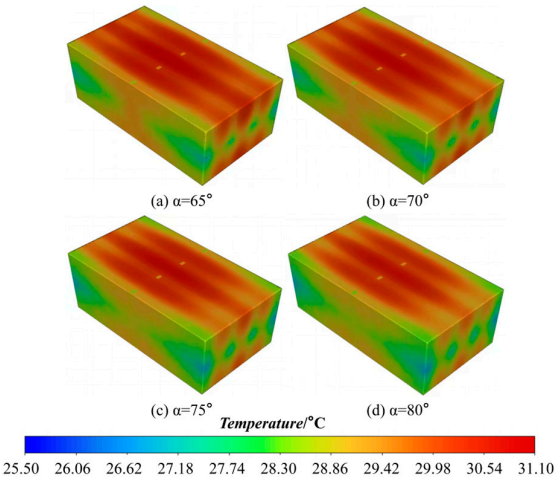

Figure 21. Temperature variation in battery for different branch channel angles.

Meanwhile, as shown in Figure 22, as the branch angle increases, the turning at the branch inlet becomes more pronounced, which increases the local losses. This leads to a slightly higher pressure gradient at the branch points, resulting in a slight increase in pressure drop. However, since the increase in pressure drop is limited and the improvement

in temperature control is more significant, we still preferred $\alpha = 80^\circ$ as the optimal value for subsequent optimization and engineering design.

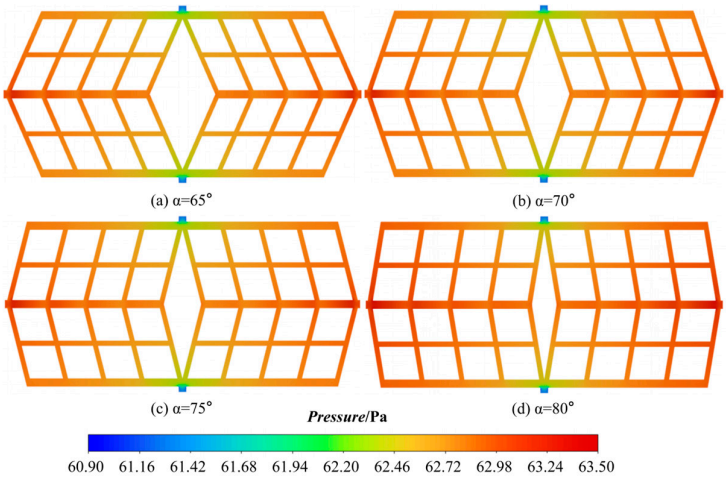

Figure 22. Variation in inlet and outlet pressure drop for different branch channel angles.

4. Orthogonal Experiment

4.1. Orthogonal Design

Based on the preliminary single-factor analyses, the factors with the most significant influence on the thermal performance of the cooling plate were identified as the main channel width (D), branch channel width (W), total channel height (H), and branch channel angle (α). These factors were subsequently incorporated into the multi-factor analysis to further quantify their relative influence on the overall thermal performance.

For the multi-factor analysis, an L16 (4^4) orthogonal experimental design was employed. L16 (4^4) denotes a 16-run orthogonal array for 4 factors, each with 4 levels. Although 4^4 theoretically yields 64 combinations, the orthogonal array selects 16 representative combinations, which efficiently capture the main effects of all factors without performing all 64 simulations. This approach enables reliable estimation of each factor's influence while saving computational resources.

The goal of the experiment was to determine the influence of these four structural factors on the performance metrics. The variation for each influencing factor is shown in Table 5. The simulation calculations were performed according to the orthogonal experimental design, and the results are summarized in Table 6.

Table 5. Orthogonal factor levels table.

Level	D (mm)	W (mm)	H (mm)	$\alpha(^\circ)$
1	1.5	1	3	65
2	2	1.5	3.5	70
3	2.5	2	4	75
4	3	2.5	4.5	80

Table 6. Orthogonal experiment calculation table.

Experiment Number	D (mm)	W (mm)	H (mm)	α(°)	T_{max}(°C)	ΔT (°C)	ΔP (Pa)
1	1.5	1	3	65	33.21	6.28	119.91
2	1.5	1.5	3.5	70	32.68	5.92	103.47
3	1.5	2	4	75	32.11	5.61	90.51
4	1.5	2.5	4.5	80	31.94	5.54	84.45
5	2	1	3.5	75	32.54	5.83	107.49
6	2	1.5	3	80	32.61	5.97	101.20
7	2	2	4.5	65	31.76	5.32	76.82
8	2	2.5	4	70	31.98	5.44	78.93
9	2.5	1	4	80	31.63	5.21	97.90
10	2.5	1.5	4.5	75	30.92	4.89	81.15
11	2.5	2	3	70	31.85	5.36	82.40
12	2.5	2.5	3.5	65	32.07	5.47	75.18
13	3	1	4.5	70	30.81	4.88	77.31
14	3	1.5	4	65	31.04	5.02	71.16
15	3	2	3.5	80	30.58	4.75	69.31
16	3	2.5	3	75	31.09	5.05	68.40

4.2. Range Analysis

This section performs a range analysis on the results of the orthogonal experiment. By comparing the R values of different factors, the significance of each factor's influence on the evaluation metrics can be clearly identified. Generally, a larger R value indicates a more significant impact of the factor's level variation on the evaluation index.

Table 7 presents the results of the range analysis based on the factors' effects on T_{max} and ΔT from Table 6. In this table, k_i represents the average value of each factor at different levels, which is used to measure the trend and intensity of the factor's impact on the evaluation index.

Table 7. Range analysis table of the orthogonal experiment.

Index	Level	D	W	H	α
T_{max}	k_1	32.485	32.048	32.190	32.020
	k_2	32.223	31.812	31.968	31.830
	k_3	31.618	31.575	31.690	31.665
	k_4	30.880	31.770	31.358	31.690
	R	1.605	0.472	0.832	0.355
ΔT	k_1	5.838	5.550	5.665	5.522
	k_2	5.640	5.450	5.492	5.400
	k_3	5.232	5.260	5.320	5.345
	k_4	4.925	5.375	5.158	5.368
	R	0.912	0.290	0.912	0.177
ΔP	k_1	99.585	100.653	90.977	85.767
	k_2	91.110	89.245	88.862	85.527
	k_3	84.157	79.740	84.625	86.887
	k_4	71.545	76.760	79.932	88.215
	R	28.040	23.912	13.045	2.688

A four-factor, four-level orthogonal experiment was designed, resulting in sixteen specific combinations for data simulation. This section further analyzes the simulation results of the orthogonal experiments listed in Table 6, using the maximum battery temperature Tmax, temperature difference ΔT, and pressure drop at the channel inlet and outlet Δp as

test indicators. For the four structural factors (main channel width D, branch channel width W, total channel height H, and branch channel angle α), the range analysis of the orthogonal experiment was applied to determine their effects on each test indicator and to investigate the variation patterns of these structural factors with respect to the three indicators.

The range calculation formulas are as follows [35,36]:

$$\begin{cases} \overline{k_{1ij}} = \frac{1}{n}\sum_1^n T_{\max} \\ \overline{k_{2ij}} = \frac{1}{n}\sum_1^n \Delta T \\ \overline{k_{3ij}} = \frac{1}{n}\sum_1^n \Delta P \end{cases} \quad (5)$$

$$Ri = \max\left\{\overline{kij}\right\} - \min\left\{\overline{kij}\right\} \quad (6)$$

where $\overline{kij}$ is the mean value of the test indicator for factor i at the j-th level, i = D/W/H/α, j =1/2/3/4, n is the number of levels, and R_i is the range of factor i.

The results of the range analysis are listed in Table 7, where k_j represents the mean value of the test results of the same factor at the same level and R is the range. The range can be used to assess the effect of each factor on the test indicators; a larger R value indicates a more significant effect, whereas a smaller R value indicates a weaker effect.

Based on the range analysis in Table 7, the influence of the four factors on the maximum temperature (Tmax) and temperature difference (ΔT) shows the following order of importance: D > H > W > α. Therefore, the optimal combination for minimizing Tmax and ΔT is D = 3 mm, W = 2 mm, H = 4.5 mm, α = 75°.

Similarly, for the pressure drop (ΔP), the order of influence is D > W>H > α, with the optimal combination for minimizing ΔP being D = 3 mm, W = 2.5 mm, H = 4.5 mm, and α = 75°.

Thus, the optimal parameters for D and H are D = 3 mm and H = 4.5 mm, while for W, as W increases from W = 2 mm to W = 2.5 mm, both Tmax and ΔT continue to decrease, while the change in ΔP is negligible, and the additional energy consumption can be ignored. Therefore, W = 2.5 mm was selected as the optimal parameter.

While the effect of α on the pressure drop is not as significant as the other three factors, its impact on Tmax and ΔT is comparable to that of α = 75° being selected as the optimal parameter. In summary, the preferred parameter combination is D = 3 mm, W = 2 mm, H = 4.5 mm, and α = 75°.

4.3. Influence of Flow Velocity Under the Optimal Parameter Combination

After optimizing the geometric parameters and determining the optimal cooling plate structure combination (D = 3 mm, W = 2 mm, H = 4.5 mm, N = 10, α = 75°), further investigation was conducted to determine the best operating conditions for this structure by studying the influence of different coolant inlet velocities on the battery thermal management performance.

As shown in Figure 23, with the increase in inlet velocity from 0.1 m·s^{-1} to 0.2 m·s^{-1}, the cooling performance of the system improved significantly. The maximum temperature (T_{max}) decreased from 30.84 °C to 29.85 °C, and ΔT reduced from 5.26 °C to 4.48 °C, showing a considerable drop in temperature. However, when the flow velocity was further increased from 0.25 m·s^{-1} to 0.3 m·s^{-1}, the improvement in cooling performance became less significant, indicating that the system had entered the "diminishing returns zone" of convective heat transfer. Increasing fluid flow velocity beyond this point did not significantly affect the heat transfer on the battery surface.

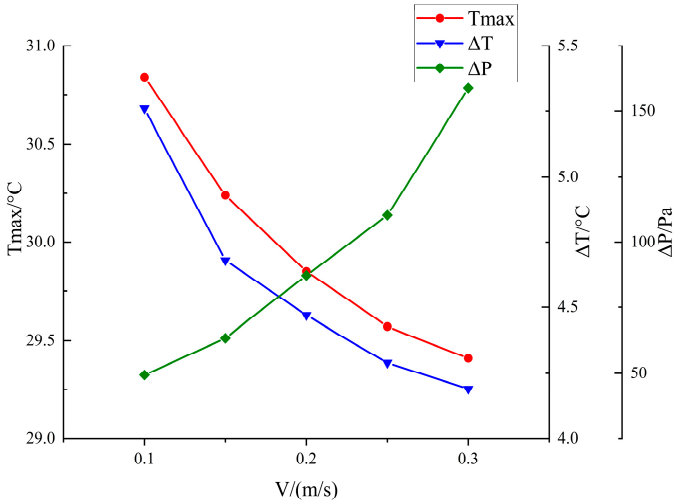

Figure 23. Variation in T_{max}, ΔT, and ΔP with inlet velocity.

In contrast to the temperature parameters, the pressure drop (ΔP) showed a noticeable increase with the increase in flow velocity. As the velocity increased from 0.2 m·s^{-1} to 0.3 m·s^{-1}, ΔP rapidly rose from 89.7 Pa to 158.77 Pa.

In summary, a flow velocity of 0.2 m·s^{-1} resulted in the optimal temperature control, with T_{max} = 29.85 °C and ΔT = 4.48 °C, while the pressure drop was 89.21 Pa, which is within an acceptable range. This represents the best balance between heat dissipation performance and energy consumption. Therefore, setting the coolant inlet velocity to V = 0.2 m·s^{-1} under the optimal structural parameters is the most reasonable choice, as it satisfies both efficient heat dissipation and energy consumption control.

5. Conclusions

To significantly enhance the thermal management performance of lithium-ion batteries in agricultural electric forklifts under complex operating conditions, this study proposed a bidirectional parallel liquid cooling plate based on a bio-inspired leaf-vein structure. A combination of single-factor and multi-factor analyses was employed to systematically evaluate the influence of key structural parameters on the thermal distribution, temperature uniformity, and channel pressure within the BTMS. The core objective of the single-factor analysis was to identify the parameters with the most significant impact on the cooling plate performance and to observe the variations in thermal distribution and internal pressure under different factor levels. Subsequently, multi-factor orthogonal experiments were conducted to quantify the relative influence of each parameter, providing clear guidance for structural optimization.

Under practical constraints, relatively optimal flow channel parameters were determined, ensuring the thermal management performance of the BTMS. Parameter selection considered both manufacturing feasibility and overall system constraints. Thermodynamic modeling served as the primary methodology, and the systematic parameter analysis enabled the identification of critical factors and quantification of their relative contributions, laying a foundation for further optimization.

The optimized bio-inspired leaf-vein flow channel structure and analysis methodology are not only applicable to lithium-ion battery thermal management but also provide reference for the design of thermal management systems in other types of energy storage devices. For instance, fuel cells, supercapacitors, or other battery systems can benefit from adopting the flow channel optimization concepts and parameter analysis approach proposed here to improve heat distribution uniformity and cooling efficiency. Furthermore, the key parameters identified through single-factor and multi-factor analyses, along with their

influence on thermal performance, can serve as a theoretical basis and design reference for structural optimization in similar energy storage devices, offering guidance and inspiration for thermal management research and engineering design across various systems.

This study still has limitations: the optimization results were obtained under standard ambient temperature conditions (25 °C) and did not explore the broader design space or extreme values of critical parameters. In future work, advanced optimization methods such as multi-objective genetic algorithms (NSGA-II) and machine learning-based surrogate models will be employed to further investigate high-impact parameters, with the aim of further optimizing BTMS thermal management performance and validating their engineering feasibility and practical applicability.

Author Contributions: Conceptualization, Z.Y.; methodology, Z.Y.; software, Z.Y.; validation, Z.Y.; formal analysis, Z.Y.; investigation, Y.W.; resources, Z.Y.; data curation, Y.W.; writing—original draft preparation, Z.Y.; writing—review and editing, B.F.; supervision, D.Y.; project administration, D.Y.; funding acquisition, D.Y. All authors have read and agreed to the published version of the manuscript.

Funding: This research was funded by the Foreign Cooperation Program of Fujian Provincial Science and Technology Department of China, grant number 2024I1006, and the Key Technology Innovation Project and Industrialization Project of Fujian Province Industrial and Information Technology Bureau (Joint Project between Universities and Enterprises), grant number 2024XQ010. The APC was funded by Fujian Province Industrial and Information Technology Bureau.

Institutional Review Board Statement: Not applicable.

Informed Consent Statement: Not applicable.

Data Availability Statement: All data presented in this study were obtained through numerical simulations and are not readily accessible. If needed, raw data files may be requested from the corresponding author.

Conflicts of Interest: The authors declare no conflicts of interest.

References

1. Tong, Z.; Guan, S. Developing high-precision battery electric forklift driving cycle with variable cargo weight. *Transp. Res. Part D Transp. Environ.* **2024**, *136*, 104443. [CrossRef]
2. Ghobadpour, A.; Monsalve, G.; Cardenas, A.; Mousazadeh, H. Off-road electric vehicles and autonomous robots in agricultural sector: Trends, challenges, and opportunities. *Vehicles* **2022**, *4*, 843–864. [CrossRef]
3. Un-Noor, F.; Wu, G.; Perugu, H.; Collier, S.; Yoon, S.; Barth, M.; Boriboonsomsin, K. Off-road construction and agricultural equipment electrification: Review, challenges, and opportunities. *Vehicles* **2022**, *4*, 780–807. [CrossRef]
4. Shang, Y.; Huang, Y.; Li, L.; Wu, F.; Chen, R. Electrochemical energy storage toward extreme conditions: Driving human exploration beyond current boundaries. *Chem. Rev.* **2025**, *125*, 5674–5744. [CrossRef] [PubMed]
5. Chen, S.; Wei, X.; Zhang, G.; Wang, X.; Zhu, J.; Feng, X.; Dai, H.; Ouyang, M. All-temperature area battery application mechanism, performance, and strategies. *Innovation* **2023**, *4*, 100465. [CrossRef]
6. Feng, Y.; Zhou, L.; Ma, H.; Wu, Z.; Zhao, Q.; Li, H.; Zhang, K.; Chen, J. Challenges and advances in wide-temperature rechargeable lithium batteries. *Energy Environ. Sci.* **2022**, *15*, 1711–1759. [CrossRef]
7. Zhu, W.; Lei, F.; Zhong, H.; Jiang, X. Thermal performance revival of composite PCM for hybrid BTMSs by architecture and formula integrated optimization. *Appl. Therm. Eng.* **2022**, *210*, 118320. [CrossRef]
8. Afia, S.E.; Cano, A.; Arévalo, P.; Jurado, F. Energy sources and battery thermal energy management technologies for electrical vehicles: A technical comprehensive review. *Energies* **2024**, *17*, 5634. [CrossRef]
9. Zhang, G.; Xiong, W.; Xie, J.; Li, X. An energy-saving battery thermal management system coupling phase change material with dynamic liquid cooling. *Int. Commun. Heat Mass Transf.* **2025**, *169*, 109815. [CrossRef]
10. Naghavi, M.; Metselaar, H.; Ang, B.; Zamiri, G.; Esmailzadeh, A.; Nasiri-Tabrizi, B. A critical assessment on synergistic improvement in PCM based thermal batteries. *Renew. Sustain. Energy Rev.* **2021**, *135*, 110259. [CrossRef]

11. Mehling, H.; Brütting, M.; Haussmann, T. PCM products and their fields of application—An overview of the state in 2020/2021. *J. Energy Storage* **2022**, *51*, 104354. [CrossRef]
12. Akbarzadeh, M.; Kalogiannis, T.; Jaguemont, J.; Jin, L.; Behi, H.; Karimi, D.; Beheshti, H.; Van Mierlo, J.; Berecibar, M. A comparative study between air cooling and liquid cooling thermal management systems for a high-energy lithium-ion battery module. *Appl. Therm. Eng.* **2021**, *198*, 117503. [CrossRef]
13. Kong, D.; Peng, R.; Ping, P.; Du, J.; Chen, G.; Wen, J. A novel battery thermal management system coupling with PCM and optimized controllable liquid cooling for different ambient temperatures. *Energy Convers. Manag.* **2020**, *204*, 112280. [CrossRef]
14. Kong, W.; Zhu, K.; Lu, X.; Jin, J.; Ni, M. Enhancement of lithium-ion battery thermal management with the divergent-shaped channel cold plate. *J. Energy Storage* **2021**, *42*, 103027. [CrossRef]
15. Zhang, Y.; Zuo, W.; Li, J.; Li, Q.; Sun, K.; Zhou, K.; Zhang, G. Performance comparison between straight channel cold plate and inclined channel cold plate for thermal management of a prismatic LiFePO4 battery. *Energy* **2022**, *248*, 123637. [CrossRef]
16. Chen, K.; Chen, Y.; Song, M.; Wang, S. Multi-parameter structure design of parallel mini-channel cold plate for battery thermal management. *Int. J. Energy Res.* **2020**, *44*, 4321–4334. [CrossRef]
17. Monika, K.; Datta, S.P. Comparative assessment among several channel designs with constant volume for cooling of pouch-type battery module. *Energy Convers. Manag.* **2022**, *251*, 114936. [CrossRef]
18. Wang, J.; Liu, X.; Liu, F.; Liu, Y.; Wang, F.; Yang, N. Numerical optimization of the cooling effect of the bionic spider-web channel cold plate on a pouch lithium-ion battery. *Case Stud. Therm. Eng.* **2021**, *26*, 101124. [CrossRef]
19. Rong, Y.; Wang, L.; Wu, T.; Yin, C.; Li, X.; Yu, X. Numerical investigation of heat transfer and parameter coupling characteristics for Spider web microchannel topological structure. *Int. J. Thermofluids* **2023**, *17*, 100307. [CrossRef]
20. Sheng, L.; Zhang, H.; Su, L.; Zhang, Z.; Zhang, H.; Li, K.; Fang, Y.; Ye, W. Effect analysis on thermal profile management of a cylindrical lithium-ion battery utilizing a cellular liquid cooling jacket. *Energy* **2020**, *220*, 119725. [CrossRef]
21. Yang, W.; Zhou, F.; Liu, Y.; Xu, S.; Chen, X. Thermal performance of honeycomb-like battery thermal management system with bionic liquid mini-channel and phase change materials for cylindrical lithium-ion battery. *Appl. Therm. Eng.* **2021**, *188*, 116649. [CrossRef]
22. Deng, T.; Ran, Y.; Zhang, G.; Yin, Y. Novel leaf-like channels for cooling rectangular lithium ion batteries. *Appl. Therm. Eng.* **2019**, *150*, 1186–1196. [CrossRef]
23. Tian, X.-W.; Wang, W.; Li, P.; Sun, C.; Wang, C.-S.; Qian, S.-H.; Wang, M. Free-shape modeling and optimization for cold plates with tree-like channels. *Int. J. Mech. Sci.* **2023**, *245*, 108076. [CrossRef]
24. Sheng, L.; Su, L.; Zhang, H.; Li, K.; Fang, Y.; Ye, W.; Fang, Y. Numerical investigation on a lithium ion battery thermal management utilizing a serpentine-channel liquid cooling plate exchanger. *Int. J. Heat Mass Transf.* **2019**, *141*, 658–668. [CrossRef]
25. Chen, Z.; Hong, X.; Huo, Z.; Ruan, D. Enhancing lithium-ion battery cooling efficiency through leaf vein-inspired double-layer liquid cooling plate design. *J. Energy Storage* **2024**, *88*, 111584. [CrossRef]
26. Chen, C.-Y.; Yang, M.; Li, Y.; Lu, G. Enhancing heat dissipation and temperature uniformity of microchannel heat sinks using fractal gradient honeycomb-reverse Tesla valve configuration. *Case Stud. Therm. Eng.* **2025**, *72*, 106371. [CrossRef]
27. Saleh, Z.M.; Al-Haidari, S.R. Numerical investigation of the effect of central inlet–dual outlet arrangement and sidewall fin shapes on the thermal-hydraulic performance of multi-channels cold plate. *Int. Commun. Heat Mass Transf.* **2026**, *173*, 110835. [CrossRef]
28. Chen, J.; Xu, W.; Tian, H.; Cao, Y.; Gu, J.; Zhou, H.; Jin, Y. Review on Lithium-Ion Battery Heat Dissipation Based on Microchannel–PCM Coupling Technology. *Energies* **2025**, *18*, 631. [CrossRef]
29. Lee, H.; Park, S.; Kim, C.W. Electrochemical–Thermal Fluid Coupled Analysis and Statistical Analysis of Cooling System for Large Pouch Cells. *Mathematics* **2024**, *12*, 3261. [CrossRef]
30. Akbarzadeh, M.; Kalogiannis, T.; Jaguemont, J.; He, J.; Jin, L.; Berecibar, M.; Mierlo, J.V. Thermal modeling of a high-energy prismatic lithium-ion battery cell and module based on a new thermal characterization methodology. *J. Energy Storage* **2020**, *32*, 101707. [CrossRef]
31. Bernardi, D.; Pawlikowski, E.; Newman, J. A general energy balance for battery systems. *J. Electrochem. Soc.* **1985**, *132*, 5–12. [CrossRef]
32. Lyu, C.; Song, Y.; Yang, D.; Wang, W.; Ge, Y.; Wang, L. Online prediction for heat generation rate and temperature of lithium-ion battery using multi-step-ahead extended Kalman filtering. *Appl. Therm. Eng.* **2023**, *231*, 120890. [CrossRef]
33. Yao, F.; Guan, X.; Chen, Q.; Lin, L. Research on thermal management system of lithium-ion battery with a new type of spider web liquid cooling channel and phase change materials. *J. Energy Storage* **2024**, *81*, 110447. [CrossRef]
34. Albana, M.H.; Batubara, N.H.; Novebriantika, N.; Silalahi, M.T.; Yogantara, Y.; Guntur, H.L. Investigation of Flow Channel Configurations in Liquid-Cooled Plates for Electric Vehicle Battery Thermal Management. *World Electr. Veh. J.* **2025**, *16*, 536. [CrossRef]

35. Niu, Z.H.; Pang, K.G.; Pang, B.B.; Wang, S. Orthogonal experimental-based thermal management design and simulation optimization of a liquid-cooled battery module. *Sci. Rep.* **2025**, *15*, 33442. [CrossRef]
36. Xin, Q.; Yang, T.; Zhang, H.; Zeng, J.; Xiao, J. Simulation and Optimization of Lithium-Ion Battery Thermal Management System Integrating Composite Phase Change Material, Flat Heat Pipe and Liquid Cooling. *Batteries* **2023**, *9*, 334. [CrossRef]

Disclaimer/Publisher's Note: The statements, opinions and data contained in all publications are solely those of the individual author(s) and contributor(s) and not of MDPI and/or the editor(s). MDPI and/or the editor(s) disclaim responsibility for any injury to people or property resulting from any ideas, methods, instructions or products referred to in the content.